RESEARCH ARTICLE

Compact Measurement Apparatus for 3D Spherical Read Range Characterization of Chipless RFID

ZESHAN ALI[1] **AND ETIENNE PERRET**[1,2], (Senior Member, IEEE)
[1]Univ. Grenoble Alpes, Grenoble INP, LCIS, 26000 Valence, France
[2]Institut Universitaire de France, 75005 Paris, France

Corresponding author: Zeshan Ali (zeshanali@outlook.fr)

ABSTRACT In the literature, chipless RF identification (RFID) tags are mostly characterized at normal incidence, where the 3D spherical reading zone of chipless RFID tags has not been characterized. In this paper, compact measurement systems for the characterization of scatterers in 3D spherical read range are presented. Customized support structures are realized for the commercial multi-probe measurement system StarLab from MVG to construct the 3D spherical bistatic and monostatic measurement systems. A graphical user interface (GUI) is programmed to control the measurement systems and to perform postprocessing of the measurements. Owing to these measurement setups, 3D characterizations of three scattering objects are presented: an aluminum sphere, a nondepolarizing rectangular loop based chipless RFID tag, and a depolarization RF Elementary Particle (REP) chipless RFID tag. The measurement setups are capable to characterize any lightweight scatterer.

INDEX TERMS 3 dimensional, compact, measurement apparatus, polarimetric radar, radar cross section, scatterer.

I. INTRODUCTION

Practical implementation of chipless RF identification (RFID) technology [1] requires the characterization of the potential 3D spherical reading zone of chipless RFID tags. For this purpose, a suitable measurement bench of chipless RFID tags is needed. Compact antenna test ranges and radar cross section (RCS) measurement ranges are in use for many years for the experimental measurements and characterization of scattering objects. These compact test ranges can be classified into two categories: the outdoor ranges [2], [3], and the indoor ranges [4]. Many institutions have built indoor compact ranges. For example, the European Microwave Signature Laboratory [4], the Ohio State University [5], the Georgia Institute of Technology [6], the University of Pretoria [7], and the MIT Lincoln Laboratory [8]. Generally,

The associate editor coordinating the review of this manuscript and approving it for publication was Fabrizio Santi.

in these compact ranges, a spherical wave from the feed source is transformed into a plane wave incidence on the target by using the dielectric lens or reflector system [9]. According to IEEE recommendations [10], the common reflectors for indoor compact ranges are, for example, an offset parabolic reflector, dual cylindrical parabolic reflectors, Cassegraine dual reflector, and Gregorian dual reflector. The ideal features of a bistatic RCS measurement facility are listed in [11]: 1) Precise alignment of the target. 2) Good antenna polarization discrimination and port-to-port isolation. 3) High repeatability of the measurements (large signal to noise ratio). 4) Ability to change the bistatic angles. 5) Handling a wide variety of objects. 6) Easiness of measurement apparatus. The compact indoor RCS measurement facilities are normally application specific and each RCS measurement facility might not possess all ideal features due to the cost and the availability of space. For example, the reflector system (to make the plane wave incidence) might not be needed for

a measurement facility dedicated to the RCS measurements of the resonant objects which are electrically very small (e.g., chipless RFID tags).

Spherical measurement systems are capable of measuring 3D patterns (or RCS) and characterizing the antennas. Such spherical measurement systems can be realized using multi-probe technology (e.g., Satimo [12] and MVG StarLab [13]) or using a multi-axis robotic arm (e.g., 3 axis robot [14], [15] and 6 axis robot [16] [18]).

In the literature, partial reading zone of the chipless RFID tags has been characterized: tag moving on a conveyor belt [19], at different stepped positions [20], tag moving within $30\times30\times30$ cm^3 volume [21], tag at various aspect angles (including within $20\times20\times20$ cm^3 volume) [22], tag rotating in E and H planes of reading antenna [23], and tag oriented at different elevation and azimuth angles [24]. In all these works, the tags are placed in a plane perpendicular to the direction of the antenna. None of these works presents the characterization of the entire 3D spherical reading zone of the chipless RFID tags, i.e. depending on the elevation and azimuth angles.

In this paper, customized 3D spherical measurement systems are presented. These measurement systems are based on customized support structures and a commercial multi-probe measurement system StarLab from MVG [25]. First, 3D spherical characterization of a metallic sphere is presented to validate the working of the measurement system. Then, for the first time, we have presented the 3D spherical characterization (elevation and azimuth angles) of chipless RFID tags using bistatic and monostatic radar configurations. These types of measurements allow characterizing the directional dependence of the chipless RFID tags of both monostatic and bistatic configurations.

The organization of this paper is as follows. Section II presents the construction of the 3D spherical measurement setups. Section III presents the 3D spherical E-filed pattern characterization of scatterers using bistatic radar. Section IV presents 3D spherical identification results of the chipless RFID tags using bistatic and monostatic radars. Section V concludes this paper.

II. CONSTRUCTION OF 3D MEASUREMENT SETUPS

The measurement systems are mainly based on a commercial multi-probe measurement system MVG StarLab [25] and custom made supports. Fig. 1 shows the photograph of the 3D measurement equipment. Other essential parts are the transmitting (Tx) antenna, Agilent 5222A vector network analyzer (VNA), and a personal computer (PC). In our measurement systems, VNA is the source and receiver for 3D measurements. The industrial PC is connected to VNA and StarLab through a GPIB and Ethernet connection, respectively.

A. MVG StarLab

MVG StarLab is a compact and convenient antenna measurement system [see Fig. 1(inset)]. StarLab exhibits two probe arrays for the frequency band of 0.65-18 GHz arranged in
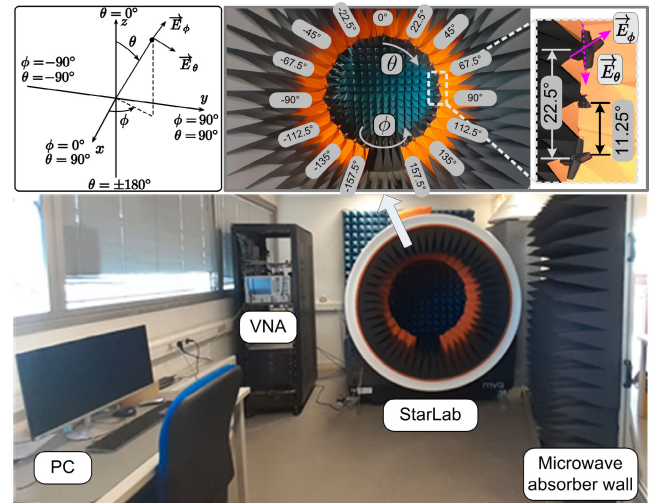

FIGURE 1. Photograph of the measurement setup based on MVG StarLab. Inset: zoom photograph of MVG StarLab.

a circular structure of diameter equals 90 cm. The probes are mounted inside the absorbers to keep the reflectivity at a minimum. Each probe is made of two linearly polarized orthogonal antennas. The first probe array of 15 dual polarized antennas operates for the frequency band of 0.65-6 GHz, while the second probe array of 14 dual polarized antennas covers the frequency band of 6-18 GHz. The angular spacing between two probes of each probe array is 22.5°. Whereas, the angular spacing between two probes of different probe arrays is 11.25°. These angularly spaced probes provide electronic scanning in elevation angle θ. The individual angles of the probes of probe array 1 are θ_n^{pa1} from -157.5° to 157.5° with step size equals 22.5° with $n = [1, 2, \ldots, 15]$. The circular arch of StarLab can rotate in a range $-11.5° \leq \theta' \leq 11.5°$ to provide mechanical elevation scanning. Therefore, electronic and mechanical scanning can be combined for full sampling in elevation angle θ. The azimuth motor provides a full sampling of azimuth angle ϕ over 360°. StarLab uses a passive combiner network that makes the system to have full reciprocity.

B. BISTATIC RADAR USING CUSTOMIZED SUPPORT STRUCTURE

The standard StarLab azimuth mast is removed and a customized support is made and attached to the azimuth motor. The customized support is mainly composed of the following parts: 1) concentric masts; 2) rotation interlocking mechanism; and 3) polystyrene stands.

Fig. 2 shows a top view [see Fig. 2(a)] and a perspective view [see Fig. 2(b)] of the concentric masts of the customized support. The outer hollow cylinder mast sits on the StarLab floor and provides the foundation for customized support. The inner hollow cylinder mast is attached to the azimuth motor of StarLab. With the hollow structure of the inner mast, an RF cable is used to connect the Tx antenna to the StarLab.
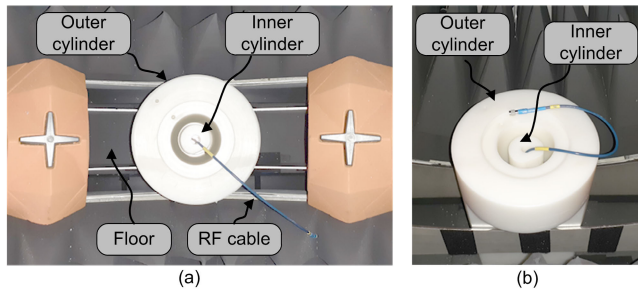
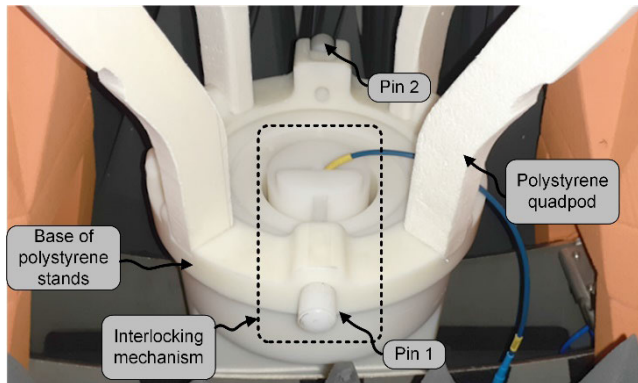**FIGURE 2.** Photographs of concentric masts of the customized support. (a) Top view. (b) Perspective view.

FIGURE 3. Photograph of the base of polystyrene stands and rotation interlocking mechanism.

TABLE 1. Three configurations of azimuth rotation.

Configuration[a]	Interlocking pin	Tx antenna	DUT	Azimuth rotation
1	none	rotate	stationary	360°
2	pin 1	stationary	rotate	180°
3	pin 2	rotate	rotate	360°

[a] The mechanical elevation scanning is reduced to a range -5° ≤ θ' ≤ 5° (as compared to the default range -11.5° ≤ θ' ≤ 11.5°)

The outer hollow cylinder mast is capped with a rotatable ring shaped structure as shown in Fig. 3. This rotatable ring shaped part acts as a base frame for the polystyrene stands that hold the device under test (DUT).

A rotation interlocking mechanism based on two pins is introduced for three configurations of azimuth rotation. These three configurations are outlined in Table 1.

The support structure is designed for two Tx antennas QH2000 (2-32 GHz) and QH800 (0.8-12 GHz). For more details about these open boundary quad-ridge horns, see [26]. A Tx antenna is placed on the inner hollow cylinder mast. For this purpose, numerous antenna bases for two antennas QH2000 and QH800 are realized as shown in Fig. 4. These antenna bases combined with the rotation interlocking mechanism provide three configurations of azimuth rotation (see Table 1) for two antennas QH2000 and QH800. The bases 1 and 6 provide configurations 1 and 3 of azimuth rotation for QH2000 and QH800 antenna, respectively. The bases 3 and 7 provide configuration 2 of azimuth rotation for QH2000 and QH800 antenna, respectively. The bases 2 and 4 provide the same functionality as base 1 and base 3 on an elevated height,
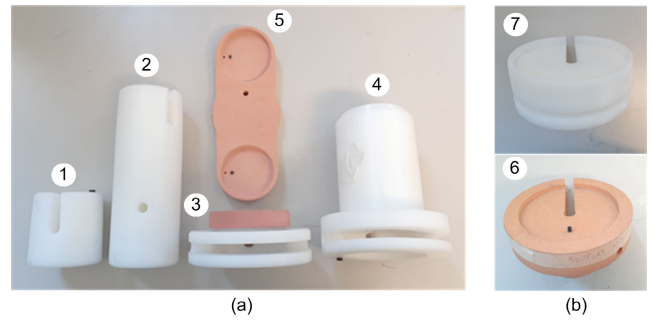

FIGURE 4. Photographs of bases for antennas. (a) QH2000. (b) QH800.
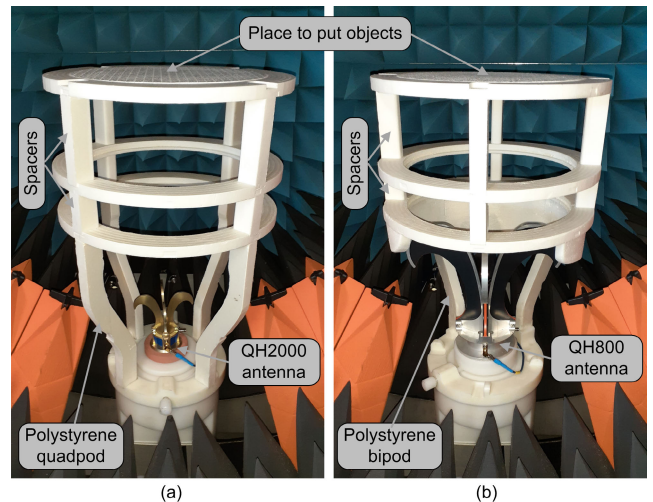

FIGURE 5. Photographs of polystyrene stands and antennas for configuration 2 of azimuth rotation. (a) Polystyrene quadpod and QH2000. (b) Polystyrene bipod and QH800.

respectively. The base 5 is supplementary to the bases 1 and 3 and made to put two QH2000 antennas.

Two polystyrene stands are realized: a polystyrene quadpod and a polystyrene bipod. The effect of polystyrene stands is electromagnetically negligible. Fig. 5 presented two measurement setups for the demonstration: 1) using polystyrene quadpod and QH2000 antenna with base 3 for configuration 2 of azimuth rotation; and 2) using polystyrene bipod and QH800 antenna with base 7 for configuration 2 of azimuth rotation. Note that polystyrene stands and antennas are interchangeable. The cable from StarLab is attached to the Tx antenna using the hollow structure of the inner mast. DUT is placed at the center of the StarLab arch on top of the Polystyrene stands. The height of the polystyrene stands can be compensated using the spacers.

Owing to the customized support, the azimuth angle ϕ rotates over 360° for azimuth rotation configurations 1 and 3 regardless of the choice of polystyrene stands (quadpod or bipod) and antennas (QH2000 or QH800). On the other hand, for azimuth rotation configuration 2, the azimuth angle ϕ rotation is limited to over 180°. This is due to less available space under the antenna base for the interlocking of the base of polystyrene stand and the inner mast (i.e., screwed to azimuth motor).
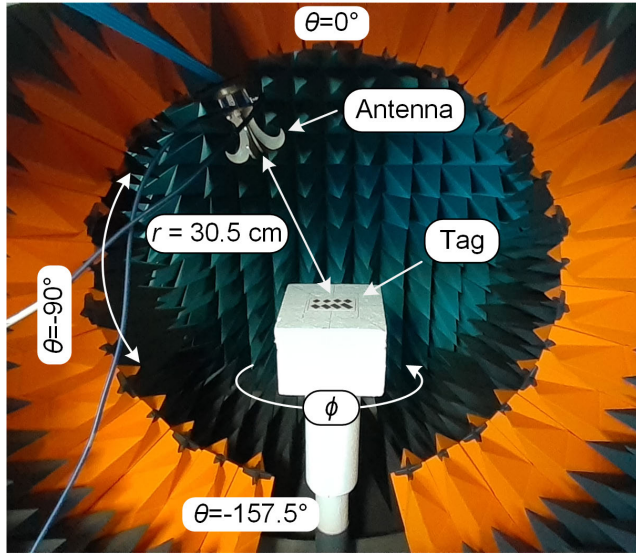
FIGURE 6. Use of StarLab as the controlled anechoic environment with the antenna connected to external wires.

The diameter of the outer mast of customized support put a constraint on the mechanical elevation scanning. Owing to the customized support, the mechanical elevation scanning is reduced to a range -5° $\leq \theta' \leq$ 5° (as compared to the default range -11.5° $\leq \theta' \leq$ 11.5°).

One additional feature of the customized support is the use of StarLab as a controlled anechoic environment for the monostatic and bistatic radar configuration with the externally connected antenna. It can be observed in Fig. 6 that the azimuth angle ϕ rotation over 180° for azimuth rotation configuration 2 is still possible even with external wires.

In this paper, we have chosen to present azimuth rotation configuration 1: Tx antenna rotates keeping the scatterer stationary (see Table 1) along with QH2000 antenna for demonstration. QH2000 antenna is chosen for its compact size and ease of handling. However, QH800 can also be used as its higher gain in the utilized frequency band generally gives better measurement accuracy. However, its larger size relative to the wavelength makes it more difficult to position the tag in the far field. The rest of azimuth rotation configurations and QH800 antenna will be utilized for future work. Fig. 7 shows the photograph of 3D spherical bistatic radar measurement setup using customized support. The source power from VNA is 0 dBm. IF bandwidth is set to a value of 10 kHz and sweep averaging of factor 5 is used. A calibration of the VNA is done up to the antenna connectors for these measurements. For the reception of the signals, probe array 1 (that comprises 15 probes) is used. The scatterer (i.e., DUT) is placed on top of the polystyrene stands at the center of the StarLab arch and the forward transmission coefficient signals in 3D are measured. The signals of the empty scene (i.e., in the absence of scatterer) are also measured in 3D to remove the clutter. For the rest of this paper, the clutter has been removed from the signals measured in the presence of the scatterer. This clutter removal is in the form of subtraction between the complex signals of scatterers and the empty scene.

C. MONOSTATIC RADAR USING 3D PRINTED ANTENNA SUPPORT

We have also setup 3D spherical measurements using monostatic radar configuration as shown in Fig. 8. For this purpose, again the azimuth motor of MVG Starlab system is used to rotate the scatterer. The entire range of azimuth angle ϕ_c is $-180° \leq \phi \leq 180°$ with $\Delta\phi$ equals 2°. One dual

FIGURE 7. Photograph of 3D spherical bistatic radar measurement setup using customized support.

polarization horn antenna QH2000 is placed on the arc with an elastic strap using a 3D printed antenna support. The position of the antenna is changed manually. The overall elevation θ_c interval is $-157.5° \leq \theta \leq 0°$ with $\Delta\theta$ equals 11.25°. Ports 1 and 2 of VNA are connected to V and H ports of the antenna, respectively. The reflection coefficient S_{11} (co-polarized component) and transmission coefficient S_{21} (cross-polarized component) are measured. Here, it is important to note that the MVG Starlab probe arrays are not used for measurements.

D. GRAPHICAL USER INTERFACE (GUI) BASED ON MATLAB

We have programmed a Matlab based acquisition graphical user interface (GUI) to control StarLab and VNA with a commercial PC. This GUI uses an application programming interface (API) provided by MVG and the virtual instrument standard architecture (VISA) based GPIB interface to control the StarLab and VNA, respectively.

The controllable VNA measurement parameters are: start and stop of frequency of sweep, number of points, IF bandwidth, sweep averaging, and selection of S parameters. The rest of the parameters (such as VNA output power, etc) are programmed directly on the VNA if required.

The controllable StarLab measurement parameters are probe array, the polarization of probes, the sweep of specific probes, azimuth angle ϕ using azimuth motor, and electronic scanning of elevation angle θ. The control of the mechanical

FIGURE 8. Photograph of 3D spherical measurement setup with monostatic radar setup.

elevation scanning is purposely not provided in GUI as a safety precaution as the range is restricted to $-5° \leq \theta' \leq 5°$. A proficient user can program it from the Matlab code of GUI. The experimental measurements are stored by using the industrial PC via the acquisition GUI.

III. 3D SPHERICAL CHARACTERIZATION OF SCATTERERS USING BISTATIC RADAR

Here, the 3D spherical bistatic radar measurement setup is utilized (see the discussion of Fig. 7). Two scatterers are used to validate the performance of the measurement setup: an aluminum sphere (a broadband scatterer) and a rectangular loop (resonant half-wavelength resonator). The photographs of these scatterers along with their geometrical dimensions are presented in Fig. 9. The diameter of the sphere is $d_s = 15$ cm. The metal sphere is insensitive to polarization alignment due to its rotational symmetry and its exact analytical solution can be calculated using the Mie Series [27]. The scattering matrix of a metal sphere is

$$S^{\text{sphere}} = \begin{bmatrix} 1 & 0 \\ 0 & 1 \end{bmatrix}. \quad (1)$$

The rectangular loops are based on a coplanar stripline (CPS) [28]. Based on the transmission line analysis provided in [29], a rectangular loop resonator is analogous to a short-circuit-terminated transmission line section. The frequency of resonance f_r of such CPS rectangular loop is:

$$f_r = \frac{c}{2\sqrt{\varepsilon_{\text{eff}}}L'}, \quad (2)$$

where $L' = L + 2\Delta L$, L' is the total length of the loop, L is the physical length of the loop, ΔL is a complementary length added due to the short circuit termination at both ends, c is the speed of light in the vacuum, and ε_{eff} is the effective permittivity for CPS [28]. The substrate is Rogers RO4003C
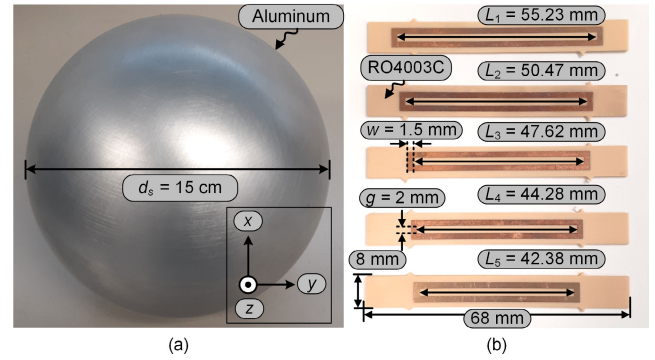
FIGURE 9. Photographs of the scatterers along with their geometrical dimensions. (a) Aluminum sphere. (b) Rectangular loops.

with dielectric permittivity $\varepsilon_r = 3.55$ and substrate height $h = 0.81$ mm. The lengths of the loop slots are $L_1 = 55.23$ mm, $L_2 = 50.47$ mm, $L_3 = 46.62$ mm, $L_4 = 44.28$ mm, and $L_5 = 42.38$ mm. The width of trace $w = 1.5$ mm. The width of slot $g = 2$ mm. The overall substrate dimensions of each loop scatterer are 68×8 mm^2.

For the experimental 3D characterization aluminum sphere (i.e., broadband scatterer), the frequency is swept from 1 GHz to 6 GHz with 1001 points. The entire range of azimuth angle ϕ_d is $-90° \leq \phi \leq 90°$ with $\Delta\phi$ equals $2°$. We have used mechanical scanning combined with electronic scanning of elevation angle θ, where the circular arch of the StarLab comprising the probes is rotated within $\theta' = \pm5°$ with a step size $\Delta\theta'$ equals $1°$. Then, the overall elevation interval $\boldsymbol{\theta}_d$ is:

$$\boldsymbol{\theta}_d = \bigcup_{n=1}^{15} \boldsymbol{I}_n, \quad (3)$$

where $\boldsymbol{I}_n$ is the subinterval of each probe within $-5° \leq \theta_n^{\text{pa1}} \leq 5°$ with a step size of $1°$.

Fig. 10 shows the measurements of the aluminum sphere at $\phi = 0°$ and $\theta = 0°$. The ϕ-polarized magnitude E-field signal E_ϕ presents co-polarized broadband scattering of the aluminum sphere. The θ-polarized magnitude E-field signal E_θ presents cross-polarized scattering with amplitude less than -35 dB because of the symmetrical shape of the aluminum sphere. Ideally, the cross polarized scattering of a metallic sphere must be null [see (1)]. However, a slight error in the light of sight alignment of Tx and Rx antennas and the metallic sphere might produce a non-null cross-polarized signal. The total magnitude E-field signal E_T is in agreement with E_ϕ showing negligible contribution of E_θ. The spherical measured total E-field E_T of the aluminum sphere at 5 GHz [see solid black line in Fig. 10] for $\boldsymbol{\phi}_d$ and $\boldsymbol{\theta}_d$ is presented in Fig. 11. The total measurements are 30030 which took a time duration of around 49 hours.

The simulations are performed using full-wave commercial software CST microwave studio. The farfield E-field monitor at 5 GHz is used. Fig. 12 presents the simulated normalized scattered E-field pattern (E_T) of the aluminum sphere at 5 GHz. It can be observed that the measurements (see
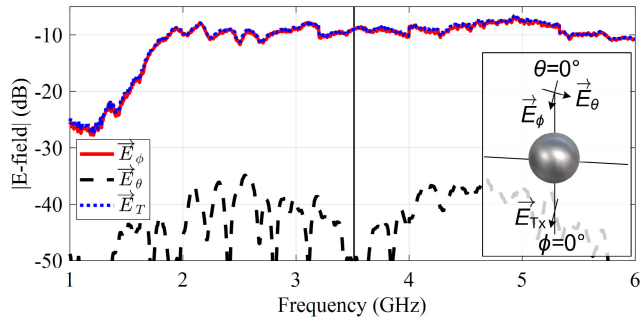
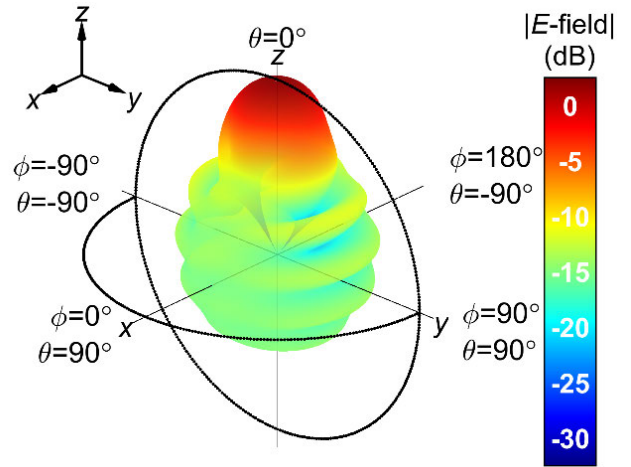**FIGURE 10.** Measured scattered E-fields of the aluminum sphere at $\phi = 0°$ and $\theta = 0°$.

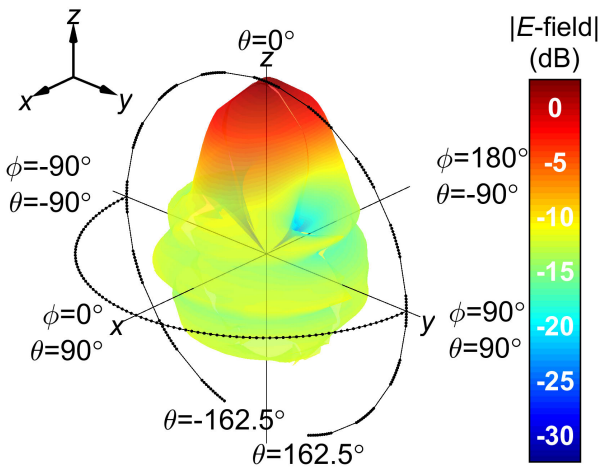**FIGURE 11.** Measured normalized scattered E-field pattern (E_T) of the aluminum sphere at 5 GHz for ϕ_d and θ_d.

FIGURE 12. Simulated normalized scattered E-field pattern (E_T) of the aluminum sphere at 5 GHz.
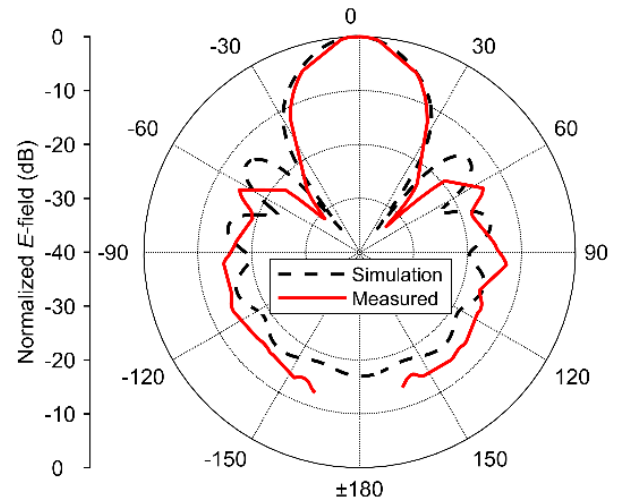
FIGURE 13. Comparison of simulated and measured scattered E-field patterns (E_T) of the aluminum sphere at elevation cut with $\phi = 90°$ at 5 GHz.

Fig. 11) are in agreement with the simulations (see Fig. 12), where the forward scattering (i.e., $\theta = 0°$) is larger than the backward scattering (i.e., $\theta = \pm 180°$). Fig. 13 presents a comparison of simulated and measured radiation patterns (in normalized amplitudes) at elevation cut with $\phi = 90°$ at 5 GHz. It can be observed that the measurements are in agreement with the simulations in the main lobe. The side-lobes exhibit shifts of a few degrees in θ. The fair values of these shifts are difficult to estimate because the fragmentary sampling of θ [see (3)] is resulting in the absence of some data points. The shifts are emerged due to human error of placing the sphere in the center of StarLab.

For the experimental 3D characterization rectangular loops, (i.e., resonant scatterer), the frequency is swept from 1.5 GHz to 3.5 GHz with 1001 points. The entire range of azimuth angle ϕ_c is -90° $\leq \phi \leq$ 90° with $\Delta\phi$ equals 1°. We have used merely the electronic scanning of elevation angle θ. Then, the overall elevation θ_c interval is -157.5° $\leq \theta \leq$ 157.5° with $\Delta\theta$ equals 22.5°.

During the spherical measurements, five different rectangular loops are used [see Fig. 9(b)]. The only difference among these rectangular loops is the length of the loops L_i to exhibit different frequencies of resonance f_r. Fig. 14 shows the measurements of the rectangular loops

at $\phi = 0°$ and $\theta = 0°$. The ϕ-polarized magnitude E-field signal E_ϕ presents co-polarized resonant scattering of the chipless RFID tag. The θ-polarized magnitude E-field signal E_θ presents cross-polarized scattering exhibiting minimal amplitude (i.e., ideally null) because of the symmetrical loop shaped resonator. The total E-field signal E_T is in agreement with E_ϕ showing negligible contribution of E_θ. The peak apexes associated with the frequencies of resonance f_r of the rectangular loops occur at 2.13 GHz, 2.27 GHz, 2.42 GHz, 2.59 GHz, and 2.71 GHz. The third rectangular loop (i.e., peak apex at 2.42 GHz) is placed in the line of sight of transmitting antenna [see the annotations Fig. 14(inset)]. For this reason, next, we will discuss the measured total magnitude scattered E-field E_T pattern (elevation and azimuth angles) at 2.42 GHz.

The spherical measured total magnitude scattered E-field pattern (E_T) of the rectangular loops at 2.42 GHz [see solid black line in the gray region in Fig. 14] for ϕ_c and θ_c is
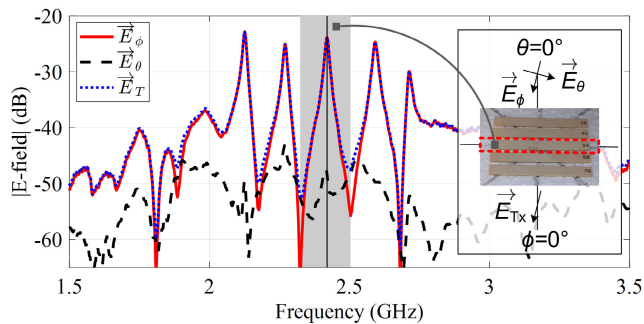
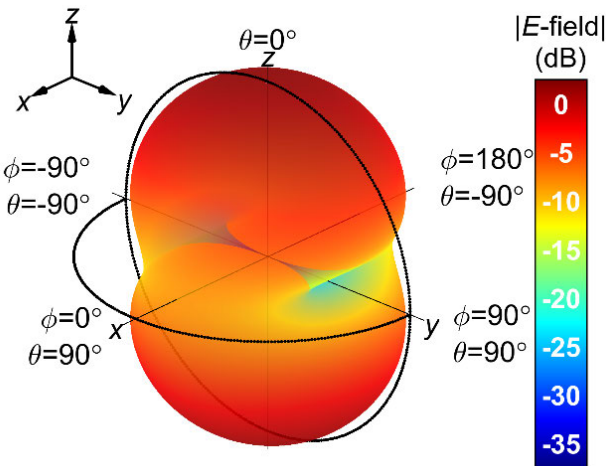**FIGURE 14.** Measured E-fields of the rectangular loops at $\phi = 0°$ and $\theta = 0°$.
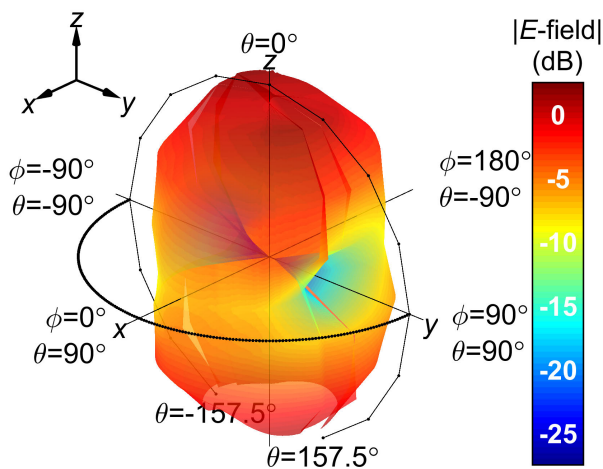

FIGURE 15. Measured normalized scattered E-field pattern (E_T) of the rectangular loops at 2.42 GHz for ϕ_c and θ_c.

presented in Fig. 15. The total measurements are 5,430 which took a time duration of around 7.5 hours.

Fig. 16 presents the simulated normalized E_T of the rectangular loops at 2.42 GHz. The 3D shape of measurements (see Fig. 15) appears in encouraging agreement with the 3D shape of simulations (see Fig. 16). However, an effective agreement can be produced by increasing the sampling in elevation angle θ. Fig. 17 presents a comparison of simulated and measured radiation patterns (in normalized amplitudes) at elevation cut with $\phi = 90°$ at 2.42 GHz. The nulls are not characterized sufficiently because of the lack of enough sampling in elevation angle θ. Conversely to the aluminum sphere, the forward scattering (i.e., $\theta = 0°$) is equal to the backward scattering (i.e., $\theta = \pm180°$) for the rectangular loops.

IV. 3D SPHERICAL IDENTIFICATION OF CHIPLESS RFID TAGS USING BISTATIC AND MONOSTATIC RADARS

Next, the characterization of the spherical reading zone of the chipless RFID is done using two measurement configurations: bistatic radar (see Fig. 7) and monostatic radar (see Fig. 8).

First, the signals are background normalized (i.e., clutter is removed) and then short-time Fourier transform (STFT) averaging [21], [22], [23], [30] is applied. A reading success

FIGURE 16. Simulated normalized scattered E-field pattern (E_T) of the rectangular loops at 2.42 GHz.
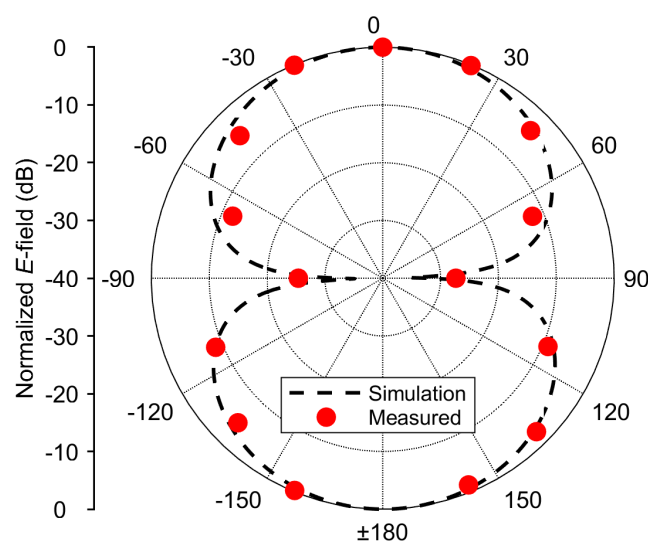
FIGURE 17. Comparison of simulated E-field pattern at 2.42 GHz and measured E-field pattern at 2.42 GHz of the rectangular loops at elevation cut with $\phi = 90°$.

happens if the frequency shifts of extracted peak apexes (associated with the resonators of the chipless RFID tag) from nominal peak apexes (see Fig. 15) are less than 50 MHz. Otherwise, it is a reading failure. In the graphs, each reading success is shown in black rectangle.

A. BISTATIC RADAR

For the bistatic radar configuration, the MVG starlab is used as described in Fig. 7. The excitation antenna as well as the probes for measuring the scattered E-field are fixed. However, the tag positioned in a plane perpendicular to the incident field rotates according to the angle ϕ. For each ϕ and θ angles, STFT spectrogram is calculated for both measured E_ϕ and E_θ using a Hamming window of 25 ns. Subsequently, two spectrograms of E_ϕ and E_θ are added and normalized. Finally, the normalized spectrogram is averaged from time $t = 140$ ns to $t = 198$ ns. A detailed discussion on the choice of the
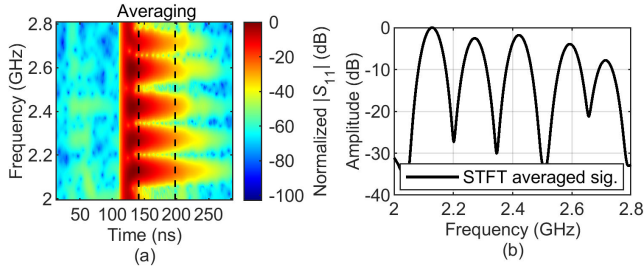
FIGURE 18. A reading success for the rectangular loops at $\phi = 0°$ and $\theta = 0°$ using bistatic radar setup Fig. 7. (a) STFT spectrogram. (b) STFT averaged signal.
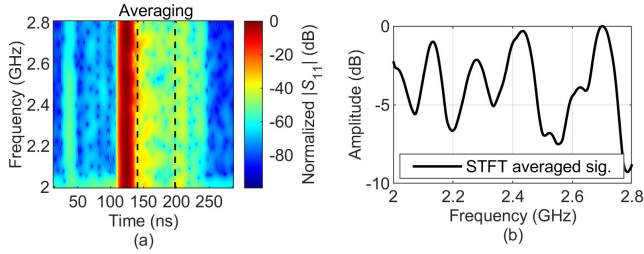

FIGURE 19. A reading failure for the rectangular loops at $\phi = 90°$ and $\theta = 157.5°$ using bistatic radar setup Fig. 7. (a) STFT spectrogram. (b) STFT averaged signal.
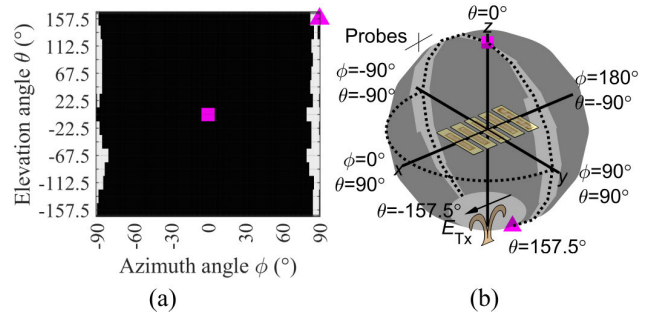

FIGURE 20. 3D identification success of the rectangular loops using bistatic radar setup (Fig. 7). (a) 2D representation. (b) 3D representation. The tag is represented in the configuration $\phi = 0$.
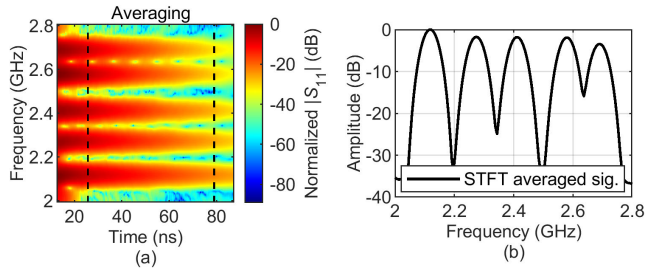

FIGURE 21. STFT averaging for the rectangular loops at $\phi = 0°$ and $\theta = -157.5°$ using monostatic radar setup (Fig. 8). (a) STFT spectrogram. (b) STFT averaged signal.

duration of the Hamming window and the STFT averaging window can be seen in [21], [22], and [30] respectively. Figs. 18 shows the calculated STFT spectrogram and STFT averaged signal for the rectangular loops at $\phi = 0°$ and $\theta = 0°$ using bistatic measurement configuration (Fig. 7). Here, the frequency shifts for all five extracted peak apexes from nominal peak apexes are less than 50 MHz; thus, it is a reading success. on the other hand, Fig. 19 presents a reading failure for the rectangular loops at $\phi = 90°$ and $\theta = 157.5°$. The absence of signal in STFT spectrogram in Fig. 19(a) in comparison to STFT spectrogram in Fig. 18(a) can be observed. Here, numerically, the frequency shifts for possible five extracted peak apexes from nominal peak apexes are larger than 50 MHz; thus, it is a reading failure.

Fig. 20 shows the 3D identification success of spherical measured E-fields E_ϕ and E_θ of the rectangular loops. Each black rectangle shows in the detection of all five peak apexes (i.e., identification success). It is observed that identification is always possible from all angle values with the exception of the region within the azimuth angle $\phi = \pm 80°$ for the entire range of elevation θ_c (see the white area). It is because, beyond $\phi = \pm 80°$, the excitation is not effective and becomes orthogonal to the loops at $\phi = \pm 90°$. This result can also be validated from the 3D radiation pattern of the rectangular loops (see Figs. 15 and 16). It can be observed that the tag reading is also possible from the rear side because these rectangular loops are single layer designs (ungrounded). Note also that the representation in Fig. 20(a) is limited to the range $-90° \leq \phi \leq 90°$, but as can be seen in Fig. 20(b), comparable results are obtained in the range $90° \leq \phi \leq 180°$. For intuitively mapping of reading success zone from 2D to 3D representation, we have superimposed two symbols in

Fig. 20: ■ and ▲ belong to $\phi = 0°$ and $\theta = 0°$, and $\phi = 90°$ and $\theta = 157.5°$, respectively. So, the signals presented in Figs. 18 and 19 are measured at the position of symbols ■ and ▲, respectively.

B. MONOSTATIC RADAR

For the monostatic radar configuration, the MVG starlab is used as described in Fig. 8. Two scatterers are characterized using this monostatic radar configuration: rectangular loops and RF Elementary Particle (REP) depolarizing chipless RFID tag.

The rectangular loops are nondepolarizing scatterers. So, STFT spectrogram is calculated for the measured reflection coefficient S_{11} (co-polarized component) using a Hamming window of 25 ns and the normalized spectrogram is averaged from time $t = 25$ ns to $t = 79$ ns. Fig. 21 shows the calculated STFT spectrogram and STFT averaged signal for the rectangular loops at $\phi = 0°$ and $\theta = -157.5°$ using monostatic measurement configuration (see Fig. 8). Here, too, the frequency shifts of all five extracted peak apexes from their corresponding nominal peak apexes are below 50 MHz, signifying a successful reading.

Using monostatic radar setup (Fig. 8), the calculated 3D spherical identification success for the rectangular loops is presented in Fig. 22. Here, too, each black rectangle shows in the detection of all five peak apexes (i.e., identification success). The position of superimposed symbol ● is exactly the same as the position of the signal presented in Fig. 21.

In the 2D representation [Fig. 22(a)], two elliptical reading failure zone are observed. At $\theta = 0°$ (when the tag is in the
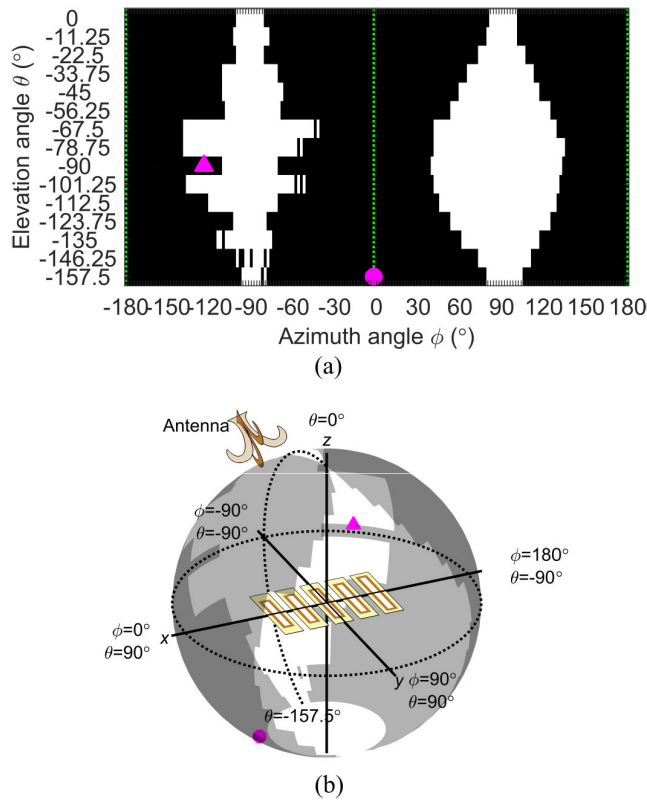
FIGURE 22. 3D spherical identification success of the rectangular loops using monostatic radar setup (Fig. 8). (a) 2D representation. (b) 3D representation. For the measurements of reflection coefficient S_{11} merely vertical polarization of the antenna is used.

FIGURE 23. STFT averaging for the rectangular loops at $\phi = 122°$ and $\theta = -90°$ using monostatic radar setup (Fig. 8). (a) STFT spectrogram. (b) STFT averaged signal.

FIGURE 24. Photograph of the depolarizing chipless RFID tag.

line of sight of the reading antenna), the reading failure zone is confined to $\pm 80° < \phi < \pm 100°$. Otherwise, the tag reading is successful. On the ϕ-axis, generally, the tag reading success zone is decreasing and increasing as the θ is ranging from $0°$ to $-90°$ and from $-90°$ to $-157°$, respectively. The worst reading success is found at $\theta = -78.75°$ in the range in the ranges of $\phi = [-180°\ -138°]$, $\phi = [-50°\ 42°]$, and $\phi = [138°\ 180°]$.

A few exceptions have happened at $\theta = -90°$, where the reading success is better than at $\theta = -78.75°$ or $\theta = -101.25°$. However, this reading success is not false positive. The measured signal at the superimposed symbol ▲ (at $\phi = 122°$ and $\theta = -90°$) is presented in Fig. 23. It can be observed that the peak apexes in the spectrogram are not strong as compared to the peak apexes in Fig. 21 but are still detectable (see Fig. 23). These unwanted reading successes might be due to the off-centered placement of the tag (human error).

It is interesting to compare the measurement results for the loops between the monostatic (Fig. 22) and bistatic (Fig. 20) configurations. It can be seen that the 3D spherical identification success zone is significantly larger for a bistatic reading when the incident field is perfectly polarized with respect to the loop.

The REP chipless RFID tag is depolarizing and grounded design as shown in Fig. 24 [31], [32]. The REP depolarizing
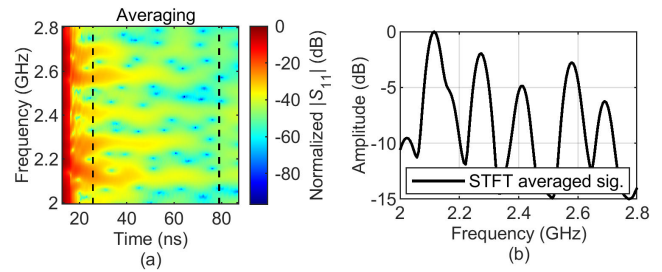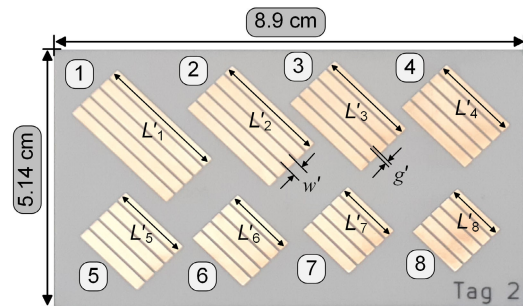
chipless tag consists of eight 45° shorted dipoles operating in ultrawideband and made up with Rogers RO4003C dielectric with permittivity $\varepsilon_r = 3.55$, and substrate height $h = 0.81$ mm. The microstrip trace width is $w' = 2$ mm and the gap between multiple coupled dipoles is $g' = 0.5$ mm. The lengths of the dipoles $L'_1 = 24.8$ mm, $L'_2 = 21.8$ mm, $L'_3 = 19$ mm, $L'_4 = 16.8$ mm, $L'_5 = 15$ mm, $L'_6 = 13.4$ mm, $L'_7 = 12.2$ mm, and $L'_8 = 11.2$ mm. The overall tag size is 8.9×5.14 cm^2. See [33, Chap. 4], for a detailed discussion on RCS levels and the bandwidths of the coupled dipoles.

The REP chipless RFID tag is composed of depolarizing scatterers. So, STFT spectrogram is calculated for the measured transmission coefficient S_{21} (cross-polarized component) using a Hamming window of 14 ns and the normalized spectrogram is averaged from time $t = 7$ ns to $t = 17$ ns. The STFT spectrogram is calculated for the frequency range from 2.8 to 6 GHz, that is, for the six resonators (from L_1 to L_6). The last two resonators (from L_7 to L_8) are omitted from the 3D spherical characterization because their signal to noise ratio (SNR) is too low at antenna to tag distance $r = 30.5$ cm. Fig. 25 shows the calculated STFT spectrogram and STFT averaged signal for the REP chipless RFID tag at $\phi = 0°$ and $\theta = 0°$ using monostatic measurement configuration (see Fig. 8). The frequency shifts observed in all six extracted peak apexes from their nominal peak apexes' values are within the range of 50 MHz, indicating a successful reading.

The calculated 3D spherical identification success for the REP depolarizing chipless RFID tag using monostatic radar setup (Fig. 8) is presented in Fig. 26. For $90° \leq \theta \leq 180°$, the reading is unsuccessful because of the ground plane of the REP chipless RFID tag. For $-90° \leq \theta \leq 90°$, the reading
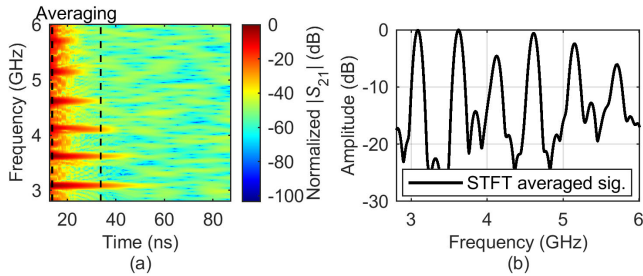
FIGURE 25. STFT averaging for the REP depolarizing chipless RFID tag at $\phi = 0°$ and $\theta = 0°$ using monostatic radar setup (Fig. 8). (a) STFT spectrogram. (b) STFT averaged signal.
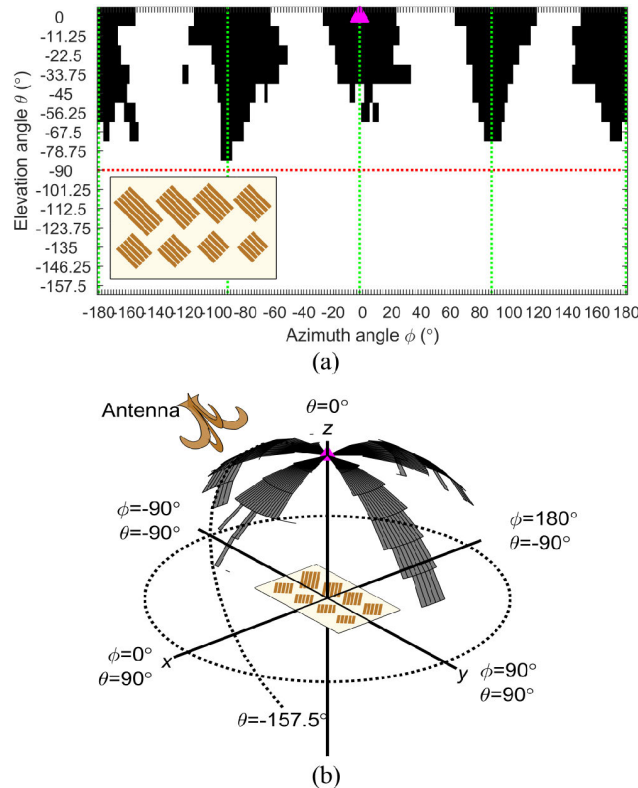

FIGURE 26. 3D spherical identification success of the chipless RFID tag using monostatic radar setup (Fig. 8). (a) 2D representation. (b) 3D representation.

successes are centered around $\phi = 0°$, $\phi = 90°$, $\phi = -90°$, and $\phi = \pm 180°$. Otherwise of these ranges, the tag reading is unsuccessful. The tag reading is only successful when the interrogation is made from the front side of the REP depolarizing tag with sufficient alignment of the excitation and reception.

It is important to note that the signal presented in Fig. 25 is measured at the position of symbol ▲.

If we compare the 3D spherical identification success area obtained between the loops and the REP chipless tag, it is clear from Figs. 24 and 26 that the coverage area is lower for the REP chipless tag. This is because the tag depolarizes the wave only at particular angles. It is noted that the coverage area of the REP tag could be increased by also considering the measured reflection coefficient S_{11}, however, this

configuration does not correspond to the one classically used for this type of tag, where the reading in cross-polarization allows to significantly increase the robustness of the reading when the tag is used in a real environment.

V. CONCLUSION

3D spherical characterizations of three scatterers (an aluminum sphere, a planner rectangular loop based chipless RFID tag, and a REP depolarization chipless RFID tag) were presented using a modified MVG Starlab system. Customized support structures were realized and their features were summarized to construct the 3D spherical bistatic and monostatic measurement systems. The comparison between the measured scattered E-field patterns and the simulated scattered E-field patterns showed a good agreement. The 3D spherical identification successes of two chipless RFID tags (rectangular loops and a REP depolarization tag) were also presented using two measurement configurations: bistatic and monostatic. These types of measurements allow characterizing the directional dependence of the chipless RFID tags. We can see from two classic examples that the coverage areas can be very different from one tag to another and that for applications, it is important to know this information in order to choose the type of resonator that best corresponds to the targeted problem. Last but not least, it was observed that the realized system is capable to characterize any lightweight scatterer.

REFERENCES

[1] E. Perret, *Radio Frequency Identification and Sensors: From RFID to Chipless RFID*. Hoboken, NJ, USA: Wiley, 2014.

[2] D.-C. Chang, C.-H. Liao, and C.-C. Wu, "Compact antenna test range without reflector edge treatment and RF anechoic chamber," *IEEE Antennas Propag. Mag.*, vol. 46, no. 4, pp. 27–37, Aug. 2004.

[3] H. C. Marlow, D. C. Watson, C. H. Van Hoozer, and C. C. Freeny, "The RAT SCAT cross-section facility," *Proc. IEEE*, vol. 53, no. 8, pp. 946–954, Aug. 1965.

[4] G. Nesti, A. J. Sieber, D. Gianfranco de Grandi, J. Fortuny-Guasch, and E. Ohlmer, "Recent advances at the European Microwave Signature Laboratory," *Proc. SPIE*, vol. 2313, pp. 1–12, Dec. 1994.

[5] E. Walton and J. Young, "The Ohio state university compact radar cross-section measurement range," *IEEE Trans. Antennas Propag.*, vol. AP-32, no. 11, pp. 1218–1223, Nov. 1984.

[6] R. Johnson, H. Ecker, and R. Moore, "Compact range techniques and measurements," *IEEE Trans. Antennas Propag.*, vol. AP-17, no. 5, pp. 568–576, Sep. 1969.

[7] D. J. J. van Rensburg and C. W. I. Pistorius, "The compact antenna test range (CATR) at the university of pretoria," in *Proc. 3D Africon Conf. Africon*, Sep. 1992, pp. 175–177.

[8] M. Shields, "The compact RCS / antenna range at MIT Lincoln Laboratory," in *Proc. 3rd Eur. Conf. Antennas Propag.*, Mar. 2009, pp. 939–943.

[9] R. B. Dybdal, "Radar cross section measurements," *Proc. IEEE*, vol. 75, no. 4, pp. 498–516, Apr. 1987.

[10] *IEEE Recommended Practice for Radar Cross-Section Test Procedures*, Standard 1502-2007, Sep. 2007, pp. 1–70, doi: 10.1109/IEEESTD.2007.4301372.

[11] C. J. Bradley, P. J. Collins, J. Fortuny-Guasch, M. L. Hastriter, G. Nesti, A. J. Terzuoli, and K. S. Wilson, "An investigation of bistatic calibration objects," *IEEE Trans. Geosci. Remote Sens.*, vol. 43, no. 10, pp. 2177–2184, Oct. 2005.

[12] P. O. Iversen, P. Garreau, and D. Burrell, "Real-time spherical near-field handset antenna measurements," *IEEE Antennas Propag. Mag.*, vol. 43, no. 3, pp. 90–94, Jun. 2001.

[13] F. Saccardi, A. Scannavini, L. Scialacqua, L. J. Foged, N. Gross, A. Gandois, S. Dooghe, and P. O. Iversen, "Virtual drive testing based on automotive antenna measurements for evaluation of vehicle-to-X communication performances," in *Proc. IEEE Int. Symp. Antennas Propag. USNC-URSI Radio Sci. Meeting*, Jul. 2019, pp. 927–928.

[14] F. Ferrero, "Spherical scanning measurement challenge for future millimeter wave applications," in *Proc. AMTA 37th Annu. Meeting Symp.*, Long Beach, CA, USA, Oct. 2015, pp. 1–7.

[15] F. Nsengiyumva, C. Migliaccio, L. Brochier, J. Dauvignac, I. Aliferis, and C. Pichot, "New *W*-band scattering measurement system: Proof of concept and results for 2-D objects," *IEEE Trans. Antennas Propag.*, vol. 66, no. 12, pp. 7224–7236, Dec. 2018.

[16] J. Hatzis, P. Pelland, and G. Hindman, "Implementation of a combination planar and spherical near-field antenna measurement system using an industrial 6-axis robot," in *Proc. AMTA*, Oct. 2016, pp. 1–6.

[17] J. R. Guerrieri, J. Gordon, D. Novotny, M. Francis, R. Wittmann, and M. Butler, "Configurable robotic millimeter-wave antenna facility," in *Proc. 9th Eur. Conf. Antennas Propag. (EuCAP)*, Apr. 2015, pp. 1–2.

[18] J. Jerauld, F. Yuen, N. Landy, and T. Driscoll, "A compact reconfigurable millimeter-wave antenna measurement system based upon an industrial robot," in *Proc. Antenna Meas. Techn. Assoc. Symp. (AMTA)*, Oct. 2019, pp. 1–6.

[19] F. Costa, M. Borgese, A. Gentile, L. Buoncristiani, S. Genovesi, F. A. Dicandia, D. Bianchi, A. Monorchio, and G. Manara, "Robust reading approach for moving chipless RFID tags by using ISAR processing," *IEEE Trans. Microw. Theory Techn.*, vol. 66, no. 5, pp. 2442–2451, May 2018.

[20] G. Khadka, M. A. Bibile, L. M. Arjomandi, and N. C. Karmakar, "Analysis of artifacts on chipless RFID backscatter tag signals for real world implementation," *IEEE Access*, vol. 7, pp. 66821–66831, 2019.

[21] R. T. de Alencar, Z. Ali, N. Barbot, M. Garbati, and E. Perret, "Practical performance comparison of 1-D and 2-D decoding methods for a chipless RFID system in a real environment," *IEEE J. Radio Freq. Identificat.*, vol. 4, no. 4, pp. 532–544, Dec. 2020.

[22] Z. Ali, E. Perret, N. Barbot, and R. Siragusa, "Extraction of aspect-independent parameters using spectrogram method for chipless frequency-coded RFID," *IEEE Sensors J.*, vol. 21, no. 5, pp. 6530–6542, Mar. 2021.

[23] A. Ramos, Z. Ali, A. Vena, M. Garbati, and E. Perret, "Single-layer, flexible, and depolarizing chipless RFID tags," *IEEE Access*, vol. 8, pp. 72929–72941, 2020.

[24] J. Alam, M. Khaliel, A. Fawky, A. El-Awamry, and T. Kaiser, "Frequency-coded chipless RFID tags: Notch model, detection, angular orientation, and coverage measurements," *Sensors*, vol. 20, no. 7, p. 1843, Mar. 2020.

[25] *MVG StarLab Website*. Accessed: Jul. 10, 2022. [Online]. Available: https://www.mvg-world.com/en/products/antenna-measurement/multi-probe-systems/starlab

[26] *Open Boundary Quad-Ridge Horns*. Accessed: May 1, 2023. [Online]. Available: https://www.mvg-world.com/en/products/antennas/measurement-probes-and-feeds/open-boundary-quad-ridge-horns

[27] G. T. Ruck, D. E. Barrick, and W. D. Stuart, *Radar Cross Section Handbook*, vol. 1. Newport Beach, CA, USA: Peninsula Publishing, 2002.

[28] R. Garg, I. Bahl, and M. Bozzi, *Microstrip Lines Slotlines*, 3rd ed. Norwood, MA, USA: Artech House, 2013.

[29] O. Rance, R. Siragusa, P. Lemaître-Auger, and E. Perret, "Contactless characterization of coplanar stripline discontinuities by RCS measurement," *IEEE Trans. Antennas Propag.*, vol. 65, no. 1, pp. 251–257, Jan. 2017.

[30] A. Ramos, E. Perret, O. Rance, S. Tedjini, A. Lázaro, and D. Girbau, "Temporal separation detection for chipless depolarizing frequency-coded RFID," *IEEE Trans. Microw. Theory Techn.*, vol. 64, no. 7, pp. 2326–2337, Jul. 2016.

[31] A. Vena, E. Perret, and S. Tedjini, "A depolarizing chipless RFID tag for robust detection and its FCC compliant UWB reading system," *IEEE Trans. Microw. Theory Techn.*, vol. 61, no. 8, pp. 2982–2994, Aug. 2013.

[32] Z. Ali and E. Perret, "Augmented depolarizing scatterer based on resonant elements for polarimetric radar calibration," *IEEE Trans. Antennas Propag.*, vol. 70, no. 2, pp. 1415–1427, Feb. 2022, doi: 10.1109/TAP.2021.3111283.

[33] O. Rance, E. Perret, R. Siragusa, and P. Lemaitre-Auger, *RCS Synth. for Chipless RFID: Theory Design*. Amsterdam, The Netherlands: Elsevier, 2017.

ZESHAN ALI received the M.S. degree in electrical engineering from King Saud University (KSU), Riyadh, Saudi Arabia, in 2015, and the Ph.D. degree in optical and radio frequency engineering from Université Grenoble Alpes, Grenoble, France, in 2019. He was a Researcher with the Department of Electrical Engineering, KSU, from 2011 to 2016, and with Laboratoire de Conception et d'Integration des Systèmes (LCIS), Grenoble-INP-Institute of Engineering, Université Grenoble Alpes, Valence, France, from 2016 to 2019. From 2019 to 2022, he was a Postdoctoral Researcher with the ScattererID Project (funded by the European Research Council (ERC) under the European Unions Horizon 2020 Research and Innovation Program) with the LCIS, Grenoble-INP-Institute of Engineering, Université Grenoble Alpes. His current research interests include chipless RFID, polarimetric radar, and RF filters. He was a recipient of the Honorable Mention from the IEEE MTT France Chapter for the Student Paper Competition at the IEEE International Microwave Symposium (IMS), Philadelphia, PA, USA, in June 2018.

ETIENNE PERRET (Senior Member, IEEE) received the Dipl.Eng. degree in electrical engineering from École Nationale Supérieure d'Électronique, d'Électrotechnique, d'Ínformatique, d'Hydraulique, et des Télécommunications, Toulouse, France, in 2002, and the M.Sc. and Ph.D. degrees in electrical engineering from the Toulouse Institute of Technology, Toulouse, in 2002 and 2005, respectively. From 2005 to 2006, he held a postdoctoral position with the Institute of Fundamental Electronics, Orsay, France. In 2006, he was appointed as an Associate Professor of electrical engineering with the Grenoble INP-Institute of Engineering, Université Grenoble Alpes, France. From 2014 to 2019, he was a Junior Member with Institut Universitaire de France, Paris, France, an institution that distinguishes professors for their research excellence, as evidenced by their international recognition. From 2015 to 2020, he was an Appointed Member of the French National Council of Universities. He has authored or coauthored more than 200 technical conferences, letters, and journal articles, and books and book chapters. He holds several patents. His works have generated more than 3500 citations. His current research interests include wireless communication systems based on the principle of backscatter modulation or backscattering of EM waves especially in the field of RFID and chipless RFID for identification and sensors, electromagnetic modeling of passive devices for millimeter and submillimeter-wave applications, and advanced computer-aided design techniques based on the development of an automated codesign synthesis computational approach. He has been a Technical Program Committee Member of the IEEE International Conference on RFID and the IEEE RFID TA. He is also a member of the IMS Technical Paper Review Committee. He was a recipient of several awards, such as the MIT Technology Review French Innovator under 35, in 2013, the French Innovative Techniques for the Environment Award, in 2013, the SEE/IEEE Leon Brillouin Award for his outstanding achievement in the identification of an object in an unknown environment using a chipless label or tag, in 2016, the IEEE MTT-S 2019 Outstanding Young Engineer Award, the Prix Espoir IMT Acadmie des Sciences, in 2020, and the Grand Prix de Electronique G Ferritin in 2021. He received an ERC Consolidator Grant for his project ScattererID, in 2017. He was a keynote speaker and the Chairperson of several international symposiums.

• • •